6th European Conference on Computational Mechanics (ECCM 6)
7th European Conference on Computational Fluid Dynamics (ECFD 7)
1115 June 2018, Glasgow, UK

INVESTIGATION OF THE MRT-LBM WITH AND WITHOUT FREE SURFACE FLOWS: VALIDATION IN CLASSICAL BENCHMARK PROBLEMS

Kenta Sato[1] **and Shunichi Koshimura**[2]

[1] Graduate School of Engineering, Tohoku University
Aoba 468-1, Aramaki, Aoba, Sendai 980-0845 JAPAN
kenta.sato.t7@dc.tohoku.ac.jp

[2] International Research Institute of Disaster Science, Tohoku University
Aoba 468-1, Aramaki, Aoba, Sendai 980-0845 JAPAN
koshimura@irides.tohoku.ac.jp

Key words: The lattice Boltzmann method, The multiple-relaxation-time model, Free surface flows, Lid-driven cavity flows, Standing waves analysis

Abstract. The lattice Boltzmann method (LBM) is an alternative simulation tool describing incompressible fluids. In recent years, it has become clear that the lattice BGK model has limitations for high-accuracy calculations. By contrast, the advanced multiple-relaxation-time (MRT) model is attracting more attention to overcome the defects of the BGK model. The objectives of this study are to verify and validate the MRT-LBM with and without free surface flows. We have performed (i) a comparison of the MRT-LBM and BGK-LBM to clarify the accuracy in two-dimensional cavity flows, (ii) a numerical simulation with the MRT-LBM's free surface model in standing waves benchmark problem. We found that the MRT-LBM has superior accuracy over the BGK-LBM in the cavity flows even in solid wall boundaries. Moreover, the MRT-LBM can controlled the compressibility drop in the 2nd order value of the Mach number in free surface flow.

1 INTRODUCTION

In recent years, the lattice Boltzmann method (LBM) has attracted attention as an alternative fluid solver. LBM can be considered to be an approach for obtaining the fluid solution of the Navier-Stokes equations. It is guaranteed that the solution is of 2nd order accuracy by Chapman-Enskog expansion, even though it can be used in low Mach number flows. The key features of LBM are as follows: (i) Fully explicit method, which means LBM does not have to solve the Poisson equation. (ii) Implementation in parallel computing is easy and can utilize high-performance computing using GPUs [1].

The most famous lattice Boltzmann equation is the lattice BGK equation using a single relaxation time [2]. Due to its simplicity, the BGK-LBM has become the most popular lattice Boltzmann collision model. However, it has some obvious defects, such as tending

to encounter stability problems in high Reynolds number flows. The multiple-relaxation-time (MRT) collision model was also developed at the same time as the BGK-LBM [3]. Compared to the BGK-LBM, one of the attractive advantages of the MRT-LBM is the improvement in the stability in high Reynolds number flows. However, few studies have focused on the MRT-LBM detailed model validation, especially in three-dimensional free surface flows.

In this paper, we simulated some benchmark problems to verify and validate the MRT-LBM. Firstly, we made a comparison between the BGK-LBM and MRT-LBM to clarify the accuracy in two-dimensional lid-driven cavity flows [4]. Secondly, we simulated the three-dimensional standing waves [5] based on the Volume-of-Fluid (VOF) approach to verify a reproducibility of the non-linear wave phenomena. The remainder of this paper is organized as follows. Section 2 briefly outlines the basic theory of the LBM. Section 3 describes the PLIC-VOF approach we used as a free surface model. Section 4 presents the model verification and validation through comparison of the MRT-LBM with BGK-LBM simulating the with and without free surface flows. Section 5 concludes the paper.

2 THE LATTICE BOLTZMANN METHOD

2.1 THE LATTICE BGK MODEL

LBM solves fluid dynamics on a mesoscopic scale by the kinematic equation for the particle distribution functions f_i. The governing equation is based on the discretized lattice Boltzmann equation, which describes the behavior of the microscopic particles.

The lattice BGK equation [2] using a single relaxation time τ is given as:

$$f_i\left(\boldsymbol{x}+\boldsymbol{e}_i\Delta t, t+\Delta t\right) = f_i\left(\boldsymbol{x}, t\right) - \frac{1}{\tau}\left[f_i\left(\boldsymbol{x}, t\right) - f_i^{eq}\left(\rho, \boldsymbol{u}\right)\right] \tag{1}$$

in which f_i^{eq} is the equilibrium particle distribution function in the i-th discrete velocity vector on each grid $\boldsymbol{e}_i$, respectively; τ determines the macroscopic fluid kinematic viscosity; and ρ and $\boldsymbol{u}$ are the macroscopic fluid density and velocity, respectively.

In the current study, we used D2Q9 or D3Q19 lattice model shown in Fig. 1 for two or three-dimensional simulation. Accordingly, $\boldsymbol{e}_i$ can be determined as;

$$\boldsymbol{e}_i = e\begin{bmatrix} 0 & 1 & 0 & -1 & 0 & 1 & -1 & -1 & 1 \\ 0 & 0 & 1 & 0 & -1 & 1 & 1 & -1 & -1 \end{bmatrix} \tag{2}$$

for D2Q9 model, and;

$$\boldsymbol{e}_i = e\begin{bmatrix} 0 & 1 & -1 & 0 & 0 & 0 & 0 & 1 & -1 & 1 & -1 & 1 & -1 & 1 & -1 & 0 & 0 & 0 & 0 \\ 0 & 0 & 0 & 1 & -1 & 0 & 0 & 1 & -1 & -1 & 1 & 0 & 0 & 0 & 0 & 1 & -1 & 1 & -1 \\ 0 & 0 & 0 & 0 & 0 & 1 & -1 & 0 & 0 & 0 & 0 & 1 & -1 & -1 & 1 & 1 & -1 & -1 & 1 \end{bmatrix} \tag{3}$$

for D3Q19 model.

where $e = \Delta x/\Delta t$ is the speed for the square lattice; Δx and Δt are the lattice size and time step interval, respectively, due to the discretization of the fluid calculation field.

The macroscopic fluid viscosity ν is defined by τ as;

$$\nu = \Delta t\Big(\tau - \frac{1}{2}\Big)c_s^2 \tag{4}$$

where $c_s = e/\sqrt{3}$ is the sound speed.

The equilibrium distribution function f_i^{eq} is defined as [6];

$$f_i^{eq}(\rho, \boldsymbol{u}) = w_i\left\{\rho + \rho_0\left[\frac{(\boldsymbol{e}_i \cdot \boldsymbol{u})}{c_s^2} + \frac{(\boldsymbol{e}_i \cdot \boldsymbol{u})^2}{2c_s^4} - \frac{(\boldsymbol{u} \cdot \boldsymbol{u})}{2c_s^2}\right]\right\} \tag{5}$$

where ρ_0 is the constant fluid density, w_i is the weight coefficient given as;

$$w_i = \begin{cases} 4/9 & (i = 1) \\ 1/9 & (i = 2, \cdots, 5) \\ 1/36 & (i = 6, \cdots, 9) \end{cases} \tag{6}$$

for D2Q9 model, and;

$$w_i = \begin{cases} 1/3 & (i = 1) \\ 1/18 & (i = 2, \cdots, 7) \\ 1/36 & (i = 8, \cdots, 19) \end{cases} \tag{7}$$

for D3Q19 model.

Eq. 5 is formed under the following conditions;

$$\frac{\|\boldsymbol{u}_{\max}\|}{c_s} \sim \mathrm{Ma} \tag{8}$$

where Ma is the Mach number.

The macroscopic density and velocity are given as the 0th and 1st order moments of the distribution function.

$$\rho = \sum_i f_i \tag{9}$$

$$\boldsymbol{u} = \frac{1}{\rho_0}\sum_i \boldsymbol{e}_i f_i \tag{10}$$

2.2 THE MULTIPLE-RELAXATION-TIME (MRT) MODEL

The simple lattice BGK model easily becomes unstable in high Reynolds number flow. We used the more advanced MRT-LBM [7] to overcome the defects of the BGK-LBM. We will describe the MRT-LBM with D3Q19 model as follows. The MRT-LBM defines the collision term $\Omega_i[f_i(\boldsymbol{x}, t)]$ as:

$$\Omega_i[f_i(\boldsymbol{x}, t)] = \mathrm{M}^{-1}\mathrm{S}[(\mathrm{M}\boldsymbol{f}) - \boldsymbol{m}^{eq}] \tag{11}$$

where M is the transformation matrix composed of 19 orthogonal basic vectors $\boldsymbol{\phi}_i\{i = 0, \ldots, 18\}$ as follows:

$$\begin{aligned}
&\phi_{0,i} = n1,\ \phi_{1,i} = \boldsymbol{e}_i^2 - e^2 \\
&\phi_{2,i} = 3\left(\boldsymbol{e}_i^2\right)^2 - 6\boldsymbol{e}_i^2 e^2 + e^4 \\
&\phi_{3,i} = e_{ix},\ \phi_{5,i} = e_{iy},\ \phi_{7,i} = e_{iz} \\
&\phi_{4,i} = \left(3\boldsymbol{e}_i^2 - 5e^2\right) e_{ix},\ \phi_{6,i} = \left(3\boldsymbol{e}_i^2 - 5e^2\right) e_{iy},\ \phi_{8,i} = \left(3\boldsymbol{e}_i^2 - 5e^2\right) e_{iz} \\
&\phi_{9,i} = 3e_{ix}^2 - \boldsymbol{e}_i^2,\ \phi_{11,i} = e_{iy}^2 - e_{iz}^2 \\
&\phi_{13,i} = e_{ix}e_{iy},\ \phi_{14,i} = e_{iy}e_{iz},\ \phi_{15,i} = e_{iz}e_{ix} \\
&\phi_{10,i} = \left(2\boldsymbol{e}_i^2 - 3e^2\right)\left(3e_{ix}^2 - \boldsymbol{e}_i^2\right),\ \phi_{12,i} = \left(2\boldsymbol{e}_i^2 - 3e^2\right)\left(e_{iy}^2 - e_{iz}^2\right) \\
&\phi_{16,i} = \left(e_{iy}^2 - e_{iz}^2\right) e_{ix},\ \phi_{17,i} = \left(e_{iz}^2 - e_{ix}^2\right) e_{iy},\ \phi_{18,i} = \left(e_{ix}^2 - e_{iy}^2\right) e_{iz}
\end{aligned} \tag{12}$$

S is the relaxation rate, and $\boldsymbol{m}^{eq}$ is the equilibrium value for each moment space. The key features of the MRT-LBM are as follows:

1. The velocity function $\boldsymbol{f}$ is transformed into the moment function $\boldsymbol{m} = \mathrm{M}\boldsymbol{f}$
2. An independent relaxation rate is used in each moment space S

The moments $\boldsymbol{m}$ are determined as:

$$\boldsymbol{m} = (\rho, e, \epsilon, j_x, q_x, j_y, q_y, j_z, q_z, 3p_{xx}, 3\pi_{xx}, p_{ww}, \pi_{ww}, p_{xy}, p_{yz}, p_{zx}, m_x, m_y, m_z) \tag{13}$$

$\boldsymbol{m}^{eq}$ is given in Eq. 15, and S is the diagonal collision matrix. The non-zero values of the matrix $s_{l,i,i}$ are determined as follows:

$$\begin{aligned}
s_{l,1,1} &= s_{l,a} \\
s_{l,2,2} &= s_{l,b} \\
s_{l,4,4} &= s_{l,6,6} = s_{l,8,8} = s_{l,c} \\
s_{l,10,10} &= s_{l,12,12} = s_{l,d} \\
s_{l,9,9} &= s_{l,11,11} = s_{l,13,13} = s_{l,14,14} = s_{l,15,15} = -\frac{1}{\tau} = s_{l,\omega} \\
s_{l,16,16} &= s_{l,17,17} = s_{l,18,18} = s_{l,e}
\end{aligned} \tag{14}$$

The parameters $s_{l,a}$, $s_{l,b}$, $s_{l,c}$, $s_{l,d}$ and $s_{l,e}$ are freely chosen in the range $[-2, 0]$. These values depend on the flow conditions, such as the initial and boundary conditions, and cannot be determined generically. We chose $s_{l,a} = s_{l,b} = s_{l,c} = s_{l,d} = s_{l,e} = -1.0$ as the moments as the relaxation rate approaches its equilibrium state, which is a reasonable way to determine these parameters [7].

The non-zero equilibrium moments $\boldsymbol{m}^{eq}$ are given as:

$$\begin{aligned}
&m_0^{eq} = \rho,\ m_3^{eq} = \rho_0 u_x,\ m_5^{eq} = \rho_0 u_y,\ m_7^{eq} = \rho_0 u_z \\
&m_1^{eq} = e^{eq} = \rho_0\left(u_x^2 + u_y^2 + u_z^2\right) \\
&m_9^{eq} = 3p_{xx}^{eq} = \rho_0\left(2u_x^2 - u_y^2 - u_z^2\right) \\
&m_{11}^{eq} = p_{zz}^{eq} = \rho_0\left(u_y^2 - u_z^2\right) \\
&m_{13}^{eq} = p_{xy}^{eq} = \rho_0 u_x u_y,\ m_{14}^{eq} = p_{yz}^{eq} = \rho_0 u_y u_z,\ m_{15}^{eq} = p_{zx}^{eq} = \rho_0 u_z u_x
\end{aligned} \tag{15}$$

3 FREE SURFACE MODEL

3.1 Competing cells status

We used the volume-of-fluid (VOF) approach to capture the interface shape. The fluid fraction value c, analogous to the VOF function, is introduced as a new macroscopic value [8]. This process is a color function in the range $[0, 1]$ and divides cells into three types:

$$\text{Cell Type} = \begin{cases} \text{Gas} & (c = 0) \\ \text{Fluid} & (c = 1) \\ \text{Interface} & (\text{otherwise}) \end{cases} \tag{16}$$

Free surface movements are performed by the interface cells' motions.

3.2 The piecewise linear interface reconstruction

We used the piecewise linear interface reconstruction (PLIC) to capture the interface shapes. Fig. 2 shows the reconstruction method in this VOF approach. In three-dimensional PLIC-VOF, the interface shapes are approximated as a trapezoid, and the line segment function is given in each interface cell as follows:

$$\boldsymbol{n} \cdot \boldsymbol{x} = n_1 x_1 + n_2 x_2 + n_3 x_3 = \alpha \tag{17}$$

where $\boldsymbol{n}$ is the unit interface normal and α is the segment from the Cartesian origin. The calculation algorithms of the PLIC are as follows:

1. Calculate the interface normal $\boldsymbol{n}$
2. Calculate the segment parameter α
3. Calculate the mass flux across the cells and advection interface cells

We will describe each algorithm in the followings.

3.3 Interface normal

Various algorithms can be used to determine the interface normal $\boldsymbol{n}$. Although this calculation is the most significant components of the PLIC, because the accuracy of the interface normal directly affects the model accuracy, we used Parker and Youngs method [9].

The interface normal $\boldsymbol{n}$ can be calculated by the gradient of the fluid fraction c as follows:

$$\boldsymbol{n} = -\frac{\nabla c}{\|\nabla c\|} \tag{18}$$

The gradient is discretized by the central difference scheme from the surrounding values:

$$\nabla c = \frac{1}{2\Delta x} \begin{pmatrix} \bar{c}_x\,(x+1, y, z) - \bar{c}_x\,(x-1, y, z) \\ \bar{c}_y\,(x, y+1, z) - \bar{c}_y\,(x, y-1, z) \\ \bar{c}_z\,(x, y, z+1) - \bar{c}_z\,(x, y, z-1) \end{pmatrix} \tag{19}$$

where $\bar{c}$ is the average fraction level of neighboring cells as:

$$\bar{c}_x(x,y,z) = \sum_{i=-1}^{1}\sum_{j=-1}^{1} c(x, y+i, z+j)\cdot w_{i,j} \tag{20}$$

$$\bar{c}_y(x,y,z) = \sum_{i=-1}^{1}\sum_{j=-1}^{1} c(x+i, y, z+j)\cdot w_{i,j} \tag{21}$$

$$\bar{c}_z(x,y,z) = \sum_{i=-1}^{1}\sum_{j=-1}^{1} c(x+i, y+j, z)\cdot w_{i,j} \tag{22}$$

where $w_{i,j}$ is the weighting parameter. The following weights achieve the best accuracy.

$$w_{i,j} = \begin{cases} 4 & (i,j) = (0,0) \\ 2 & (i,j) = (1,0),(0,1) \\ 1 & (i,j) = (\pm 1, \pm 1) \end{cases} \tag{23}$$

3.4 Interface segment parameter

Various algorithms can be used to determine the segment parameter α, such as iterative root finding. All algorithms must produce the same result in this calculation step when the interface normal $\boldsymbol{n}$ is known. We used analytical algorithms [10].

First, we standardized the calculated interface normal $\boldsymbol{n}$ as $n_1 > 0$, $n_2 > 0$, $n_3 > 0$ and $n_1 + n_2 + n_3 = 1$. When the interface normals were negative values, we transformed the coordinates to the normal non-negative. Second, we calculated the inverse problem $\alpha = f'(c, \boldsymbol{n})$ by utilizing the fact that the fluid fraction c is a function of the interface normal n and the segment parameter α as follows:

$$c(\alpha, \boldsymbol{n}) = \frac{1}{6 n_1 n_2 n_3}\left[\alpha^3 - \sum_{i=1}^{3} F_3(\alpha - n_i \Delta x_i) + \sum_{i=1}^{3} F_3(\alpha - \alpha_{\max} + n_i \Delta x_i)\right] \tag{24}$$

We determined α by solving the cubic equations analytically, where $\alpha_{\max}$ is the summation of the standardized interface normal as:

$$\alpha_{\max} = n_1 + n_2 + n_3 \tag{25}$$

and F is the Heaviside function defined as:

$$F_3(x) = \begin{cases} x^3 & (x > 0) \\ 0 & (x \le 0) \end{cases} \tag{26}$$

3.5 Advection of the interface cell

In the VOF method, we have to solve the following equation to advect the fluid fraction c as:

$$\frac{\partial c}{\partial t} + \boldsymbol{u} \cdot (\nabla c) = 0 \tag{27}$$

We used the Lagrangian-explicit method [11, 12] in the interface cells to discretize Eq. 27. Fig. 3 shows a schematic illustration of the method. In this method, the surface, which is approximated by line ab, moves to line cd with the face velocity at the next time step. The blue area in Fig. 3 is the outgoing mass flux toward the right-hand cell in the next time step. As a result, the fluid fraction c^{t+1} can be determined by the incoming and outgoing mass flux as follows:

$$c_i^{t+1} = VL_{i+1} + VC_i + VR_{i-1} \tag{28}$$

where VL is the mass flux toward the left-hand cell, VR is the mass flux toward the right-hand cell, and VC is the remaining mass flux. Finally, we used the operator-splitting method for multi-dimensional advection to redetermine the interface normal $\boldsymbol{n}$ of every advection for each axis.

4 VERIFICATION & VALIDATION

4.1 Lid-driven cavity flows

This numerical simulation was conducted to clarify the accuracy between the BGK-LBM and MRT-LBM. The critical Reynolds number of the two-dimensional lid-driven cavity flow is from 8000 to 8050 within less than 1% of error [13]. The numerical simulation has been performed until $Re = 7500$ to focus on the steady state solutions in the comparison. The number of computing points is 256×256 using D2Q9 model. This variable is common to both collision models.

Fig. 4 compares the dimensionless velocity components of the u_x and u_y profiles in the steady state along vertical and horizontal center lines. In the cases of $Re = 100$ and $Re = 400$, both the BGK-LBM and MRT-LBM are in good agreement with the results of the reference [4]. In the low Reynolds number, the BGK-LBM can be applicable and satisfy the accuracy requirement with a 256×256 grid calculation.

The BGK-LBM , however, disagrees with the results [4] because the Reynolds number is increasingly high. This tendency is particularly strong near the solid wall boundary. We confirmed that the 1st order bounce-back boundary condition with the BGK-LBM is difficult for conducting high-accuracy simulations even when the Reynolds number is smaller than the critical number in this benchmark.

In contrast, the MRT-LBM results are in good agreement with the results [4] regardless of the increase of the Reynolds number. The results near the wall boundary do not decrease in accuracy; therefore, it is shown that the 1st order bounce-back boundary condition with the MRT-LBM can satisfy the accurate no-slip wall boundary condition in this simulation. It is assumed that the parameters that affect the accuracy boundary

condition are set correctly in the relaxation rates. Accordingly, the MRT's relaxation rates must be determined by each flow field. The validation of the relaxation rates except for lid-driven cavity flow is an issue for future work. Moreover, there is a possibility that the BGK-LBM can perform a high-accuracy computation if the number of computing grids is larger. It is not advisable because the calculation time increases.

Through the model comparison, it is concluded that the MRT-LBM is capable of higher accuracy calculations compared to the BGK-LBM in lid-driven cavity flows, particularly near the no-slip boundary.

4.2 Standing waves analysis

Standing waves in rectangular tank were simulated to validate our model using D3Q19 model. In this benchmark problem, Wu and Taylor [5] have calculated an analytical solution by non-linear water wave theory in second order accuracy. Fig. 5 shows calculation domain and initial settings and calculation parameters we set. The simulation was carried out for 5 seconds. The time step interval Δt was determined to satisfy Ma ~ 0.01. The maximum magnitude of the velocity was calculated by the wave speed $\sqrt{gH}$, where g is the gravity acceleration and H is the still water depth.

Fig. 6 shows the interface shapes of our model. Besides, Fig. 7 shows the Timeseries of water level at the center of the tank and spacing density profile at $t = 0.5\,(\mathrm{s})$. The key feature of 2nd order solution is that the 1st and 3rd crests are higher that 2nd one. This is caused by the non-linear effects of waves. Hence, the phenomena can not seen in first order solution because that is based on linear theory. Our model reproduced non-linear effects well and succeeded in avoiding artificial oscillations near interface cells. Moreover, the weak compressibility decreases at smaller Mach numbers, and the density decreases in $O\left(\mathrm{Ma}^2\right)$. Our model controlled the compressibility and approximates the incompressible flows well, determining the time step interval Δt by Mach numver with the required accuracy. On the other hand, our model leave room for improvement to enhance a energy conservation because the water level was damped after $t = 3.0\,(\mathrm{s})$.

5 CONCLUSIONS

In this paper, we performed verification and validation of the MRT-LBM in classical benchmark problems with and without free surface flows. The following conclusions were drawn from the discussions above:

- We found that the MRT-LBM can overcome the defects of the BGK-LBM, such as the accuracy of the no-slip boundary condition and the disturbance of fluid density.
- We substantiated that the weak compressibility in the MRT-LBM can be controlled within $O\left(\mathrm{Ma}^2\right)$ by choosing a time step interval based on the maximum velocity magnitude in the flow field.

Through the verification and validation, it is clear that the MRT-LBM might require finer resolution than that of other CFD solves. The adaptive mesh refinement technique will be needed to execute more efficient simulations.

ACKNOELEDGMENT

This study was supported by KAKENHI (Grants-in-Aid for Scientific Research) 16K12845, 17J06615.

REFERENCES

[1] P. R. Rinaldi, E. A. Dari, M. J. Vénere, and A. Clausse. A Lattice-Boltzmann solver for 3D fluid simulation on GPU. *Simul. Model. Pract. Theory*, 25:163–171, 2012.

[2] Y. H. Qian, D. D'humières, and P. Lallemand. Lattice BGK Models for Navier - Stokes equation. *Europhys. Lett.*, 17(6):479–484, 1992.

[3] P. Lallemand and L. S. Luo. Theory of the lattice Boltzmann method: Dispersion, dissipation, isotropy, Galilean invariance, and stability. *Phys. Rev. E*, 61(6):6546–6562, 2000.

[4] U. Ghia, K. N. Ghia, and C. T. Shin. High-Re solutions for incompressible flow using the Navier-Stokes equations and a multigrid method. *J. Comput. Phys.*, 48(3):387–411, 1982.

[5] G. X. Wu and R. Eatock Taylor. Finite element analysis of two-dimensional non-linear transient water waves. *Appl. Ocean Res.*, 16(6):363–372, 1994.

[6] X. He and L. S. Luo. Lattice Boltzmann Model for the Incompressible Navier-Stokes Equation. *J. Stat. Phys.*, 88(3/4):927–944, 1997.

[7] J. Tölke, S. Freudiger, and M. Krafczyk. An adaptive scheme using hierarchical grids for lattice Boltzmann multi-phase flow simulations. *Comput. Fluids*, 35(8-9):820–830, 2006.

[8] N. Thürey and U. Rüde. Stable free surface flows with the lattice Boltzmann method on adaptively coarsened grids. *Comput. Vis. Sci.*, 12(5):247–263, 2009.

[9] J. E. Pilliod and E. G. Puckett. Second-order accurate volume-of-fluid algorithms for tracking material interfaces. *J. Comput. Phys.*, 199(2):465–502, 2004.

[10] R. Scardovelli and S. Zaleski. Analytical Relations Connecting Linear Interfaces and Volume Fractions in Rectangular Grids. *J. Comput. Phys.*, 164(1):228–237, 2000.

[11] E. Aulisa, S. Manservisi, R. Scardovelli, and S. Zaleski. A geometrical area-preserving Volume-of-Fluid advection method. *J. Comput. Phys.*, 192(1):355–364, 2003.

[12] E. Aulisa, S. Manservisi, R. Scardovelli, and S. Zaleski. Interface reconstruction with least-squares fit and split advection in three-dimensional Cartesian geometry. *J. Comput. Phys.*, 225(2):2301–2319, 2007.

[13] C. H. Bruneau and M. Saad. The 2D lid-driven cavity problem revisited. *Comput. Fluids*, 35(3):326–348, 2006.

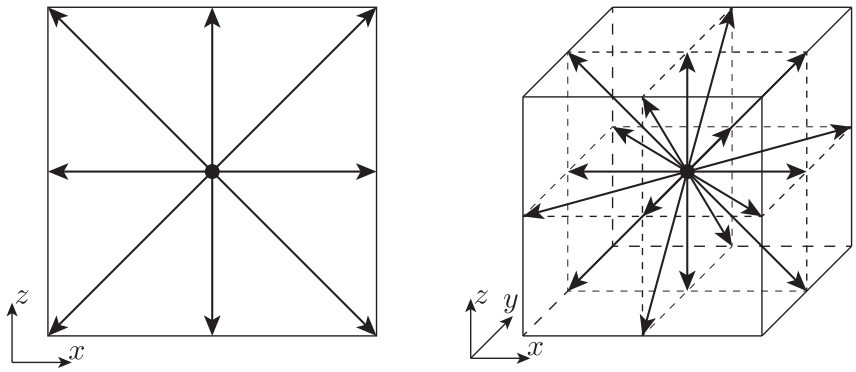

Figure 1: D2Q9 model (left), D3Q19 model (right)

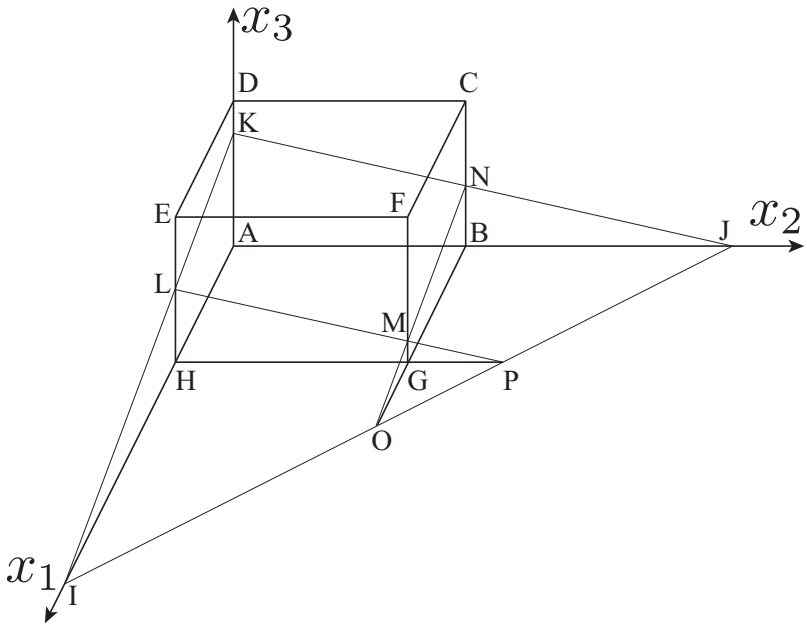

Figure 2: The cut area is the region inside the parallelepiped ABCDEFGH and below the plane IJK

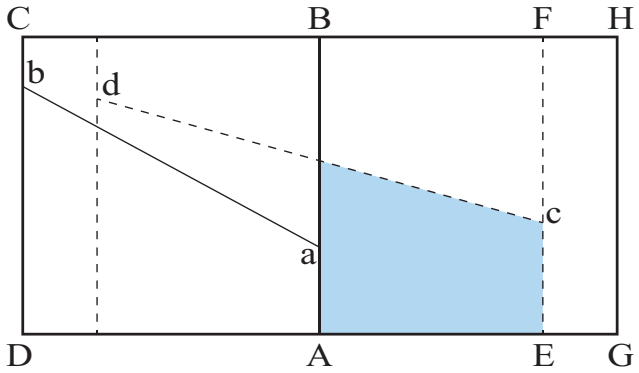

Figure 3: A schematic iilustration of the Lagrangian-Explicit method in two-dimension

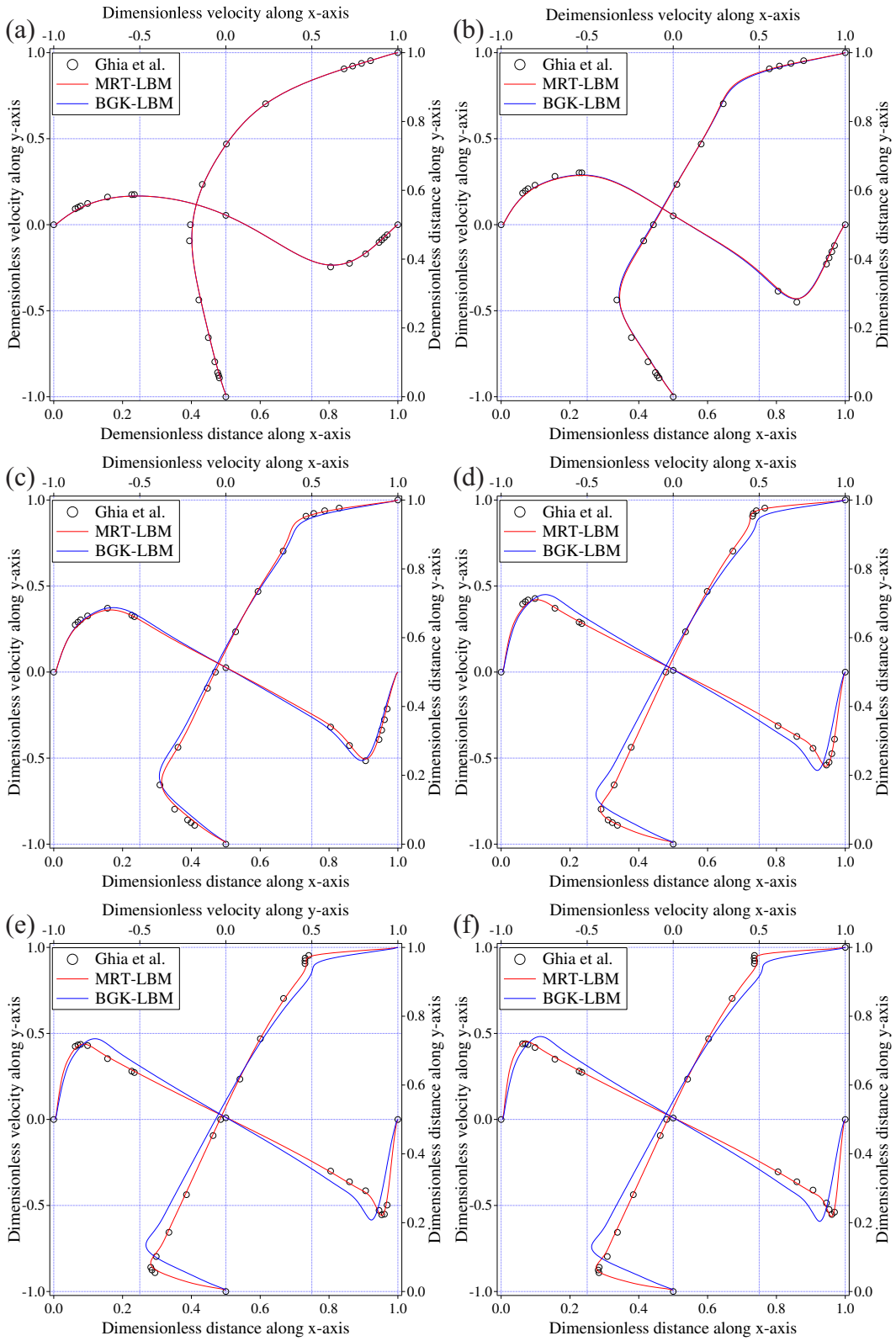

Figure 4: Dimensionless velocity profiles between the MRT-LBM and BGK-LBM in the steady state, (a)Re = 100, (b)Re = 400, (c)Re = 1000, (d)Re = 3200, (e)Re = 5000, (f)Re = 7500

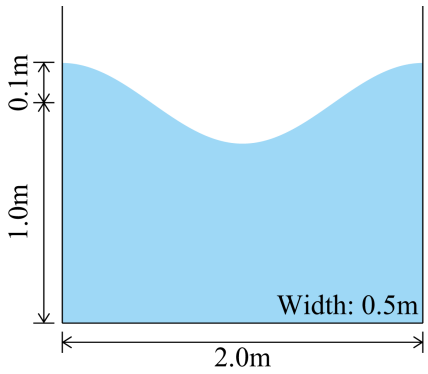

Param.	Value
Tmax	5.0s
Grid 1	100 × 25 × 75
Grid 2	200 × 50 × 150
Grid 3	400 × 100 × 300

Figure 5: The calculation domain and initial settings (left), Calculation parameters (right)

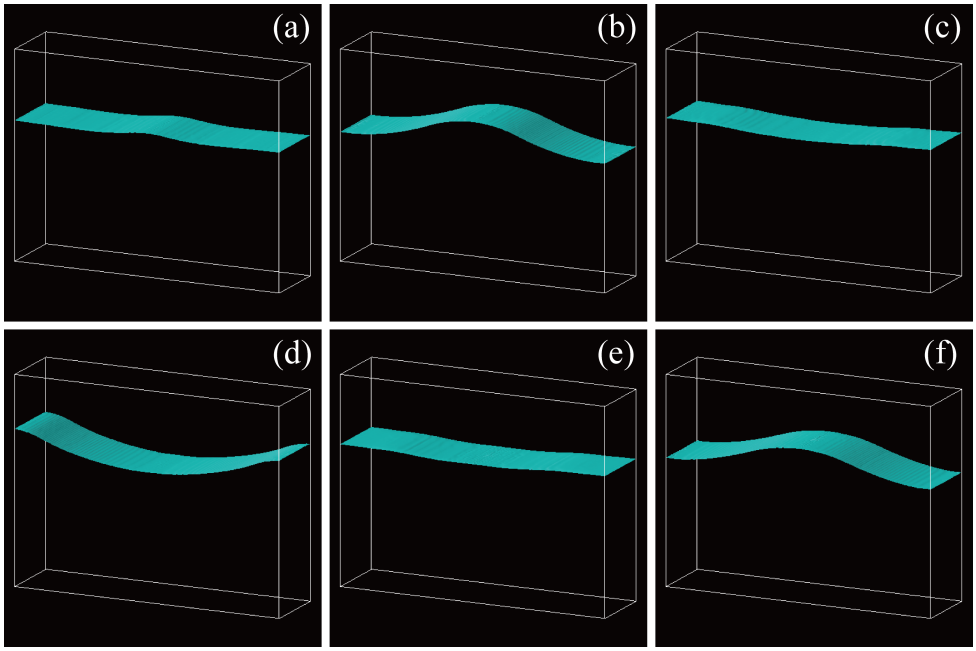

Figure 6: Interface shapes, (a) 0.3s, (b) 0.6s, (c) 0.9s, (d) 1.1s, (e) 1.4s, (f) 1.7s

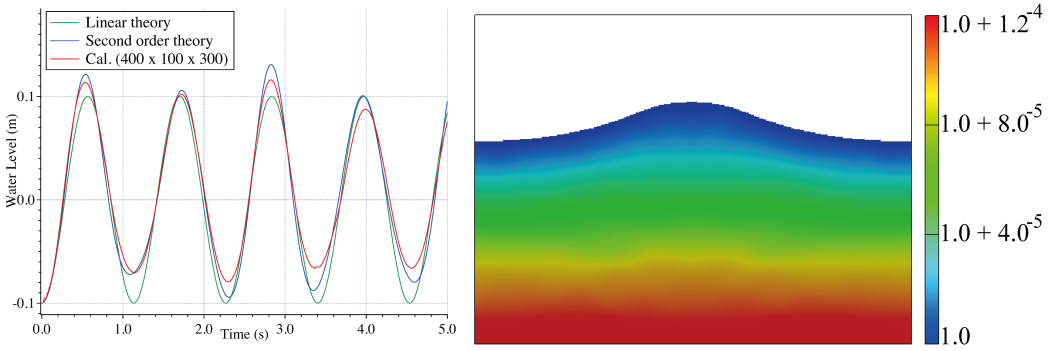

Figure 7: Timeseries of water level at the center of the tank (left), Density profiles at $t = 0.5\,(\mathrm{s})$ (right)